independently by Edward Purcell's group at Harvard (1) and Felix Bloch's group at Stanford (2) in 1946. The fundamental MRI concept was proposed by Paul Lauterbur in 1973 (3). Since then, MRI has developed into a premier tool for biomedical imaging (4).

Like many other tomographic imaging techniques (5), MRI can produce images of internal structures of an object. However, MRI is significantly different from other techniques in terms of the principles of signal generation, spatial encoding, and image contrast manipulation. This article provides an introductory description of these principles as well as some illustrative applications. For easy reference, the following is a partial list of symbols used in this article:

B_0	Static magnetic field
B_1	Radio-frequency (RF) field
G_x, G_y, G_z	Magnetic field gradients along the x, y, and z directions
B_r	Receiver sensitivity
G_{ss}	Slice-select gradient
ω_0	Larmor frequency corresponding to the B_0 field
ω_{rf}	Excitation frequency of the RF field
ω_1	Frequency of nuclear precession about the B_1 field
$\boldsymbol{i}, \boldsymbol{j}, \boldsymbol{k}$	Unit direction vectors of the x, y, and z axes
$\boldsymbol{M}$	Bulk magnetization vector
M_x, M_y, M_z	Components of $\boldsymbol{M}$
$M_{xy} \equiv M_x + iM_y$	Transverse component of $\boldsymbol{M}$ (in complex notation)
$M_{xy}(0), M_z(0)$	Post-excitation value for M_{xy} and M_z
M_z^0	Thermal equilibrium value of $\boldsymbol{M}$
$\gamma, \boldsymbol{\gamma} = \gamma/2\pi$	Gyromagnetic ratio
$h, \hbar = h/2\pi$	Planck's constant
k_B	Boltzmann's constant
I	Spin quantum number
$\boldsymbol{J}$	Angular momentum
$\boldsymbol{\mu}$	Magnetic moment vector
T_1	Longitudinal relaxation time constant
T_2, T_2^*, T_2^{**}	Transverse relaxation time constants
N_s	Total number of spins in a sample
$N_\uparrow, N_\downarrow$	Number of spins pointing up and down, respectively
$T_E = 2\tau$	Echo time
T_R	Repetition time in a multiple pulse sequence
T_I	Inversion time
τ_p	Time duration of an RF pulse
α	Flip angle
$S(t)$	Measured time signal
$\rho(\cdot)$	Spin density function
k, k_x, k_y, k_z	Spatial frequency variables
T_s	Absolute temperature of a spin system
T_{pe}	Phase encoding interval

BIOMEDICAL NMR

Magnetic resonance imaging (MRI) is a tomographic imaging technique based on the well-known nuclear magnetic resonance (NMR) phenomenon first observed in bulk materials

SIGNAL GENERATION AND CHARACTERISTICS

Generating magnetic resonance (MR) signals from a sample is the first step of the imaging process. This section discusses some of the fundamental physical concepts underlying MR signal generation.

Bulk Magnetization

It is well known that atoms consist of a nucleus surrounded by one or more orbiting electrons. The nucleus is composed of one or more positively charged protons and sometimes some neutral particles called neutrons. Protons, neutrons, electrons, and other particles possess an intrinsic angular momentum $\boldsymbol{J}$, known as spin. In the atomic nucleus, the spins of a pair of protons or neutrons often cancel each other out. As a result, only atomic nuclei with an odd number of protons and/or an odd number of neutrons have a net spin, known as nuclear spin (6). Since nuclei are charged particles, those with a nonzero nuclear spin produces a magnetic moment $\boldsymbol{\mu}$ which is related to $\boldsymbol{J}$ by (6,7)

$$\boldsymbol{\mu} = \gamma \boldsymbol{J} \tag{1}$$

where γ is a physical constant called the *gyromagnetic ratio*. The gyromagnetic ratio is nucleus-dependent. For hydrogen, $\gamma = 2.675 \times 10^8$ rad s^{-1} T^{-1} or $\boldsymbol{\gamma} = \gamma/2\pi = 42.58$ MHz/T. The nucleus of the hydrogen atom is the simplest in nature, consisting of just one proton and no neutron. Because hydrogen is the most common element found in the human body, proton MRI is widely used.

A sample has a large number of nuclear spins. The collective magnetism of a sample is represented by a bulk magnetization vector $\boldsymbol{M}$ defined as

$$\boldsymbol{M} = \sum_{n=1}^{N_s} \boldsymbol{\mu}_n \tag{2}$$

where N_s is the total number of spins. To further characterize $\boldsymbol{M}$, it is necessary to know the behavior of $\boldsymbol{\mu}$. Based on the quantum-mechanical model, the magnitude of $\boldsymbol{\mu}$, often denoted as μ, is given by

$$\mu = \gamma \hbar \sqrt{I(I+1)} \tag{3}$$

where $\hbar$ is Planck's constant h (6.6×10^{-34} J · s) divided by 2π and I is the nuclear *spin quantum number*. The spin quantum number takes integer, half-integer, or zero values such that $I = 0, 1/2, 1, 3/2, 5/2, \ldots$. For ^1H, ^{13}C, ^{19}F, and ^{31}P nuclei, $I = 1/2$, and such a spin system is called a spin-$\frac{1}{2}$ system. A nucleus is NMR-active only if $I \neq 0$.

While the magnitude of $\boldsymbol{\mu}$ is certain, its direction is randomized under the thermal equilibrium condition due to thermal random motion. Therefore, $\boldsymbol{M} = 0$ in the absence of an external magnetic field. To activate nuclear magnetism from a sample, we need to place the sample in a strong external magnetic field, often referred to as the B_0 field, which is produced by the main magnet in an MRI system. The behavior of $\boldsymbol{\mu}$ in the presence of B_0 is summarized as follows.

First, the orientation of $\boldsymbol{\mu}$ is quantized along the direction of the external field while its orthogonal component still points to a random direction (6,7). To see this more clearly, consider a spin-$\frac{1}{2}$ system and assume that B_0 points along the z direction such that

$$\boldsymbol{B}_0 = B_0 \boldsymbol{k} \tag{4}$$

where $\boldsymbol{k}$ is the unit direction vector of the z axis. The z component of $\boldsymbol{\mu}$ will take one of two possible values. That is,
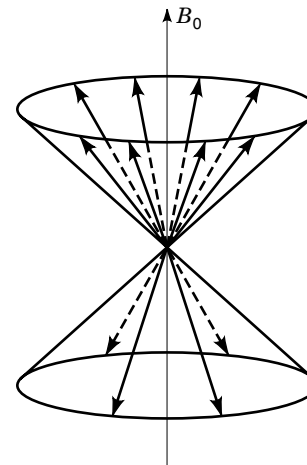

Figure 1. Distribution of nuclear magnetic moments in the presence of the B_0 field for a spin-$\frac{1}{2}$ system.

$$\mu_z = \pm \gamma \hbar / 2 \tag{5}$$

which corresponds to two spin states: pointing up (parallel) or pointing down (anti-parallel), as illustrated in Fig. 1. The transverse component μ_{xy}, however, points in a random direction. Second, $\boldsymbol{\mu}$ precesses about the B_0 field, as described by the following equation of motion:

$$\frac{d\boldsymbol{\mu}}{dt} = \gamma \boldsymbol{\mu} \times \boldsymbol{B}_0 \tag{6}$$

The precessional frequency, known as the natural resonant frequency of a spin system, is given by the well-known Larmor equation:

$$\omega_0 = \gamma B_0 \tag{7}$$

Clearly, given a spin system, its resonant frequency is determined by the magnetic field that it experiences. A group of spins with the same resonant frequency is called an *isochromat*.

Third, the population difference among different spin states is governed by the Boltzman distribution (6,7). Specifically, for a spin-$\frac{1}{2}$ system, we have

$$\frac{N_\uparrow}{N_\downarrow} = \exp\left(\frac{\Delta E}{k_B T_s}\right) \tag{8}$$

where $N_\uparrow$ and $N_\downarrow$ denote the number of spins pointing up and down, respectively, such that $N_s = N_\uparrow + N_\downarrow$, $\Delta E = \gamma \hbar B_0$ is the energy difference between the two spin states ($E_\downarrow - E_\uparrow$), k_B is the Boltzmann constant (1.38×10^{-23} J/K), and T_s is the absolute temperature of the spin system. Noting that

$$\boldsymbol{M} = (N_\uparrow - N_\downarrow)\mu_z \boldsymbol{k} \tag{9}$$

and replacing the exponential function in Eq. (8) by its first-order approximation yields

$$\boldsymbol{M} = \frac{\gamma^2 \hbar^2 B_0 N_s}{4 k_B T_s} \boldsymbol{k} \tag{10}$$

Two points are evident from the above equations. First, M points along the direction of the applied magnetic field. Second, the magnitude of M is directly proportional to the external magnetic field strength and the total number of spins (N_s). The value of N_s is characteristic of a sample being imaged and cannot be changed in general. The only controllable parameters are B_0 and T_s. Therefore, for a given spin system, one can increase the magnitude of M by increasing B_0 or decreasing T_s. Since MRI experiments are often carried out in human subjects, one is limited to increasing the magnitude of the applied magnetic field for an increase in the bulk magnetization. The optimal field strength for imaging is application-dependent. For most clinical MRI systems, B_0 ranges from 0.2 T to 2 T.

RF Excitation

The presence of a bulk magnetization does not directly imply the generation of a measurable NMR signal. In fact, M is basically unmeasurable because M appears to be stationary in the laboratory reference frame when it lies parallel to the B_0 field. The next step in MR signal generation is, therefore, to tip it away from the z axis so that the torque of the B_0 field exerted on M will force it to precess about the B_0 field; consequently, the precessing M will induce an electrical signal in a receiver coil.

Tipping M is accomplished by exciting the spin system with a time-varying magnetic field, known as the B_1 field. A simple, circularly polarizing B_1 field is given, in complex notation, by

$$B_1(t) = B_{1,x}(t) + iB_{1,y}(t) = B_1 e^{-i\omega_{rf} t}, \qquad 0 \le t \le \tau_p \quad (11)$$

where ω_{rf} is the excitation frequency and τ_p is the time duration for which the B_1 field is turned on. In practice, ω_{rf} is chosen according to the so-called on-resonance condition that $\omega_{rf} = \omega_0$, and τ_p is selected based on the desired frequency content of the B_1 field. Because ω_{rf} is in the RF range and τ_p is on the order of microseconds to milliseconds, the excitation B_1 field is commonly called an RF pulse.

The excitation effect of an RF pulse is conveniently described in the rotating reference frame (x', y', z') (8,9), in which the transverse plane is precessing in the same fashion as the B_1 field. In this frame, the B_1 field appears to be a static field pointing along the x' axis while the B_0 field "vanishes." Consequently, M precesses about the x' axis at the Larmor frequenc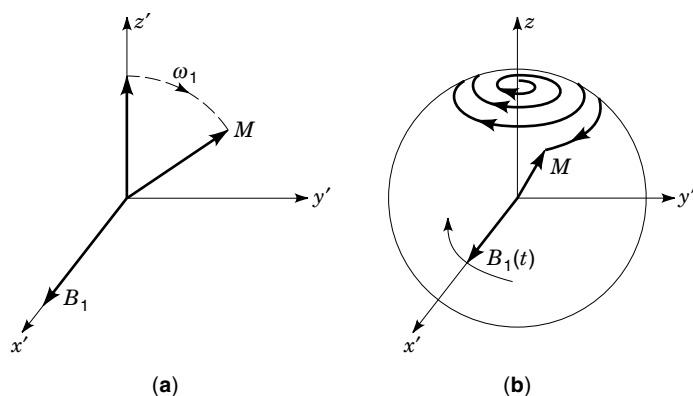y $\omega_1 = \gamma B_1$, as illustrated in Fig. 2. The tip angle between M and the z axis at the end of the pulse is

$$\alpha = \gamma B_1 \tau_p \quad (12)$$

If $\alpha = 90°$, such a pulse is called a 90° pulse. Similarly, we have 180° pulses or arbitrary α-degree pulses.

Free Precession and Relaxation

After a magnetized spin system is perturbed from the equilibrium state by an RF pulse, the spin system will return to this state provided that the B_1 field is removed and sufficient time is given. This process is characterized by a precession of M about the B_0 field, called *free precession;* a recovery of the longitudinal magnetization (M_z), called *longitudinal relaxation;* and the destruction of the transverse magnetization (M_{xy}), called *transverse relaxation*. Both relaxation processes are often ascribed to the existence of time-dependent microscopic magnetic fields surrounding a nucleus due to the random thermal motion present in a sample, but the exact mechanisms by which these relaxation events occur for an arbitrary spin system are far too diverse and complex to be properly covered here. The interested reader is referred to Ref. 7.

Phenomenologically, free precession and the relaxation processes are described by the Bloch equation (8)

$$\frac{dM}{dt} = \gamma M \times B - \frac{M_x \boldsymbol{i} + M_y \boldsymbol{j}}{T_2} - \frac{(M_z - M_z^0)\boldsymbol{k}}{T_1} \quad (13)$$

Expressing the transverse magnetization as $M_{xy} = M_x + iM_y$ and the pulse condition as $M_{xy} = M_{xy}(0)$, $M_z = M_z(0)$, and $B = B_0 \boldsymbol{k}$, the solution to the Bloch equation is given by

$$\begin{cases} M_{xy}(t) = M_{xy}(0)e^{-t/T_2}e^{-i\omega_0 t} \\ M_z(t) = M_z^0(1 - e^{-t/T_1}) + M_z(0)e^{-t/T_1} \end{cases} \quad (14)$$

where M_z^0 is the thermal equilibrium value of M, which can be calculated from Eq. (10). Note that with this model, the longitudinal component grows exponentially with time constant T_1, while the transverse component precesses about the B_0 field at the Larmor frequency and decays exponentially with time constant T_2. The electrical signal introduced in a receiver coil by the precessing M according to Faraday's law of induction is expressed by (9)

$$S(t) = -\frac{d}{dt} \int_{\text{object}} B_c(r) \cdot M(r, t) \, dr \quad (15)$$

where $B_c(r)$ describes the sensitivity of the receiver coil at different points in space. Because the time derivative of the longitudinal component M_z is much less than that of the transverse component M_{xy}, one often treats $M_{xy}(t)$ as the measured signal with the omission of various weighting factors.

Signal Characteristics

The transient electrical signal observed from a spin system immediately after a pulse excitation is called a *free induction decay* (FID) signal. Ignoring various nonessential weighting factors, an FID signal generated by an α-degree pulse can be expressed as

Figure 2. Precession of M in the presence of a rotating RF field as observed in (a) the rotating frame and (b) the laboratory frame.
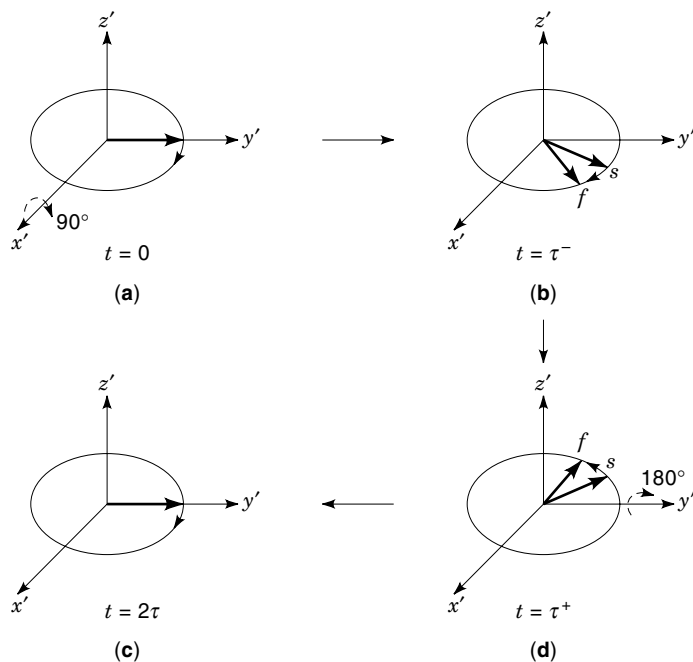
Figure 3. Vector diagram illustrating the refocusing of isochromats in a spin-echo experiment.

$$S(t) = \sin\alpha \int_{-\infty}^{\infty} \rho(\omega)e^{-t/T_2(\omega)}e^{-i\omega t}\, d\omega, \qquad t \geq 0 \qquad (16)$$

where $\rho(\omega)$ is known as the spectral density function such that $M = \int \rho(\omega)\, d\omega$. A characteristic of an FID signal is that it is a decaying signal, whose decay rate is strongly tied to the underlying spectral distribution. In the idealized case of a single spectral component, the FID signal bears a characteristic T_2 decay. This is the case when both the sample and the external magnetic field to which the sample is exposed are perfectly homogeneous. When the magnetic field is inhomogeneous, the FID signal decays at a much faster rate, characterized by a new time constant T_2^*. Specifically, if the field inhomogeneity lends itself to a Lorentzian distribution with full-width half-maximum ΔB_0, we have

$$\frac{1}{T_2^*} = \frac{1}{T_2} + \gamma\,\Delta B_0 \qquad (17)$$

Another form of MR signal is known as *echo*. A distinct difference between an echo and an FID signal is that an echo is "two-sided," with one side from the refocusing phase of a transverse magnetization and the other side from the dephasing phase.

One type of echo signal, known as spin echo or RF echo, is generated by applying multiple RF pulses (10). A simple example is the two-pulse excitation scheme consisting of a 90° pulse followed by a time delay τ, then a 180° pulse. Assume that the 90° pulse is applied along the x' axis and the 180° is applied along the y' axis and, further, that the sample has two isochromats with precessional frequencies ω_s (slow) and ω_f (fast) in the rotating frame. Ignoring any off-resonance effects, the 90° pulse rotates both magnetization vectors onto the y' axis, as shown in Fig. 3(a). After the pulse, these vectors precess about the z axis. Since one is precessing rela-

tively faster than the other, they progressively lose phase coherence as the free precession continues. After a time interval τ, the two vectors fan out in the transverse plane by a phase angle $(\omega_f - \omega_s)\tau$ as shown in Fig. 3(b). At this point, the 180° pulse is applied along the y' axis, which flips the two vectors over to the other side of the transverse plane as shown in Fig. 3(c). As a consequence, the faster vector is now lagging behind the slower by the same phase angle with which it was leading the slower prior to the 180° pulse. Since both vectors will continue to precess clockwise at angular frequencies ω_f and ω_s (assuming that the magnetic field inhomogeneity is time-invariant), the faster isochromat will "catch" the slower one after a time interval τ, thus recreating a phase coherence between the two vectors at time $t = 2\tau$ as shown in Fig. 3(d).

Although Fig. 3 shows the situation with only two isochromats, the analysis can be extended to the general case. In fact, because of the existence of a large number of isochromats in a real sample, a total dephasing normally occurs by the time the 180° pulse is applied. This means that the transverse magnetization M_{xy} completely vanishes and the FID signal disappears when the 180° pulse is applied. After the 180° pulse, M_{xy} grows gradually and reaches the maximum value at $t = 2\tau$, which is often called the echo time T_E. If we ignore the T_2 relaxation, the mechanism responsible for the loss of the phase coherence among the isochromats during the free precession period before the 180° is the same as that responsible for the recovery of the phase coherence after the pulse. Therefore, M_{xy} as a function of time possesses the following property:

$$|M_{xy}(\tau - t)| = |M_{xy}(\tau + t)|, \qquad 0 \leq t \leq \tau \qquad (18)$$

In other words, $|M_{xy}(t)|$ has a mirror symmetry about the time axis $t = \tau$. For $t > \tau$, $M_{xy}(t)$ is a recalled transverse magnetization of which the rephasing part ($\tau < t < 2\tau$) is responsible for one side of the echo signal and the subsequent dephasing part ($t > 2\tau$) responsible for the other side of the echo. In practice, the echo suffers a T_2 decay, as shown in Fig. 4, and
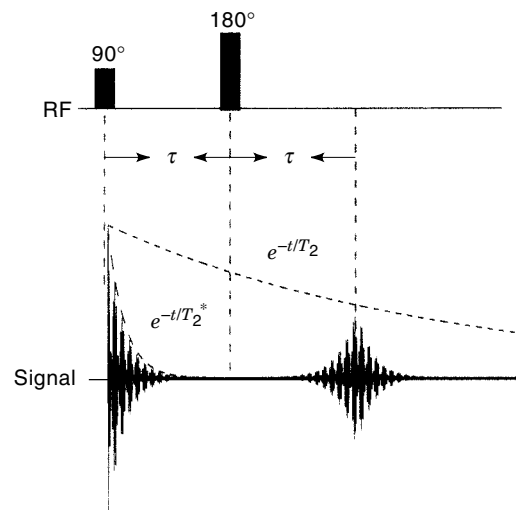

Figure 4. Formation of a spin-echo signal by a 90°–τ–180° sequence. Note that the FID signal quickly disappears as the spins dephase, and the echo signal formed after the 180° pulse carries a T_2 weighting.
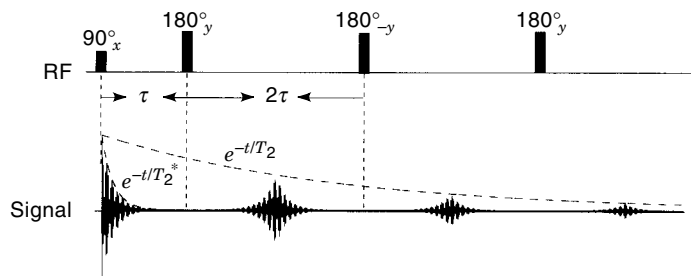
Figure 5. Formation of a train of spin echoes by multiple 180° pulses. Note that the 90° pulse is applied along the x' axis and the subsequent refocusing 180° pulses are applied alternatively along the $\pm y'$ axis as the subscripts indicate.

consequently the echo amplitude carries a characteristic T_2 weighting factor e^{-T_E/T_2}.

When a spin system is excited by a 90° pulse followed by a sequence of 180° pulses, a train of spin echoes will be generated, as shown in Fig. 5. Suppose that the 90° pulse is applied at $t = 0$ and that the 180° pulses are applied at $(2n - 1)\tau$ for $n = 1, 2, \ldots, N$. There will be a train of N echoes formed at $t = 2n\tau$, and the echo amplitudes are weighted by $e^{-2n\tau/T_2}$. Specifically, if we assume that the 90° pulse is applied along the x' axis and the subsequent refocusing 180° pulses are applied alternatively along the $\pm y'$ axis (11), the resulting signal is known as the Carr–Purcell–Meiboom–Gill (CPMG) echo train. The phase shifts between the pulses are used in this pulse sequence to reduce the effect of practical imperfections in RF pulses.

Another form of echo signal frequently used in MRI is generated using time-varying gradient magnetic fields. Such an echo is called a *gradient echo* to distinguish it from a spin echo. The key concept underlying gradient-echo formation is that a gradient field can dephase and rephase the transverse magnetization in a controlled fashion so that one or multiple echo signals can be created.

For simplicity, consider the pulse sequence in Fig. 6 in which a negative x gradient is turned on after the application of an α-degree RF pulse. It is easy to show that spins in differ-

ent x positions will acquire different phases in the rotating frame, which can be expressed as

$$\phi(x, t) = \gamma \int_0^t -G_x x \, d\tau = -\gamma G_x x t, \qquad 0 \le t \le \tau \qquad (19)$$

Clearly, the loss of spin phase coherence becomes progressively greater as time elapses after the excitation pulse. The resulting signal decay is sometimes characterized by a new time constant T_2^{**}. After a time $\tau > 3T_2^{**}$, the signal decays effectively to zero; but at this point, if a positive gradient of the same strength is applied, the transverse magnetization components will gradually rephase, resulting in a regrowth of the signal. Specifically, the spin phase function is now given by

$$\phi(x, t) = -\gamma G_x x \tau + \gamma \int_\tau^t G_x x \, dt$$
$$= -\gamma G_x x \tau + \gamma G_x x(t - \tau), \qquad \tau \le t \le 2\tau \qquad (20)$$

It is evident that the phase dispersal introduced by the negative gradient is gradually reduced over time after the positive gradient is turned on at $t = \tau$. After a time τ, the spin phase ϕ is zero for any x value, which means that all the spins have rephased and an echo signal is formed. Note that it is not necessary to set the magnitude of the refocusing gradient to be identical to that of the dephasing gradient. If a different refocusing gradient is used, the echo time will be changed accordingly. Another point worth noting is that, in contrast to spin-echo signals, gradient-echo signals carry a characteristic T_2^* decay because the phase dispersal term due to main field inhomogeneities cannot be refocused by gradient reversal.

SIGNAL LOCALIZATION

An important concept in MR signal localization is the use of magnetic field gradients. Consider the simple case that a linear gradient field is introduced along the x direction. The overall field become

$$B(x) = B_0(x) + G_x x \qquad (21)$$

and the Larmor frequency as a function of position becomes

$$\omega(x) = \omega_0(x) + \gamma G_x x \qquad (22)$$

This simple relationship is the basis of MR signal localization.

Slice Selection

Slice selection is accomplished through the use of a shaped RF pulse and a slice-select gradient. To make an RF pulse spatially selective, it is necessary to make the spin resonant frequency position dependent or, most desirably, linearly varying along the slice-select direction. An obvious way to accomplish this is to augment the homogeneous B_0 field with a linear gradient field. For example, if a gradient is applied in the z direction with an amplitude G_z, a slice of thickness Δz centered about the origin will have frequencies ranging from $-\gamma G_z \Delta z/2 + \omega_0$ to $\gamma G_z \Delta z/2 + \omega_0$. Consequently, an RF pulse with the finite frequency bandwidth $\Delta \omega = \gamma G_z \Delta z$ centered about ω_0 will just excite spins within this slice.
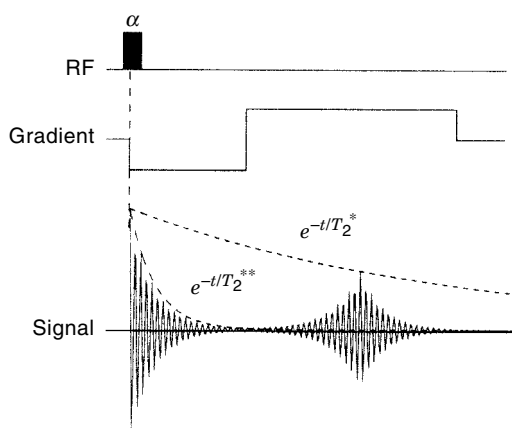

Figure 6. Formation of a gradient echo. Note that after the α-degree pulse, a negative gradient is turned on to dephase the spins, which is followed by a positive gradient to rephase the spins, thus generating an echo signal.
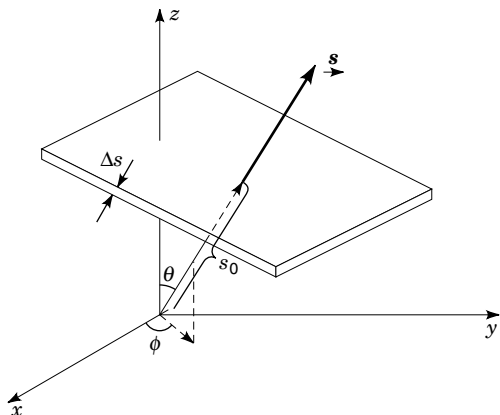
Figure 7. Parameters for characterizing a slice of arbitrary orientation.

One approach to design such a pulse is to extend the simple RF pulse in Eq. (11) to have a more general amplitude function such that

$$B_1(t) = B_1^e(t)e^{-i\omega_{rf}t} \tag{23}$$

A popular example is the sinc pulse in which $\omega_{rf} = \omega_0$, and

$$B_1^e(t) = A \operatorname{sinc}[\Delta\omega(t - \tau_p/2)], \qquad 0 \le t \le \tau_p \tag{24}$$

More sophisticated pulses can be found in Ref. 12 and references therein.

To select a slice in an arbitrary direction and location as shown in Fig. 7, we need to turn on gradients in all three directions. Specifically, representing the slice-select gradient as

$$\boldsymbol{G}_{ss} = (G_x, G_y, G_z) \tag{25}$$

the required gradient along each spatial direction is

$$\begin{aligned} G_x &= G_{ss}\sin\theta\cos\phi \\ G_y &= G_{ss}\sin\theta\sin\phi \\ G_z &= G_{ss}\cos\theta \end{aligned} \tag{26}$$

Correspondingly, the excitation frequency (ω_{rf}) and bandwidth ($\Delta\omega$) for the RF pulse are

$$\begin{aligned} \omega_{rf} &= \omega_0 + \gamma G_{ss}s_0 \\ \Delta\omega &= \gamma G_{ss}\Delta s \end{aligned} \tag{27}$$

It is clear that one can position the selected slice at will by adjusting the relative values of G_x, G_y, G_z, and the RF pulse.

Frequency-Encoding and Phase-Encoding

After a signal is generated from a region of interest, spatial information has to be encoded into the signal during the free precession period for image formation. Since an MR signal is in the form of a complex exponential, we have essentially two ways to encode spatial information: *frequency-encoding* and *phase-encoding.* Frequency encoding, as the name implies, makes the oscillating frequency of an MR signal linearly de-

pendent on its spatial origin. The physical principle used to realize this is rather simple. Consider first an idealized one-dimensional object with spin density distribution $\rho(x)$. If the magnetic field that the object sees after an excitation pulse is the homogeneous B_0 field plus another linear gradient field ($G_x x$), the Larmor frequency at position x is given in Eq. (22). Correspondingly, the signal generated locally from spins in an infinitesimal interval dx at point x, with the omission of the transverse relaxation effect, can be written as

$$dS(x,t) \propto \rho(x)\,dx e^{-i\gamma(B_0+G_x x)t} \tag{28}$$

where the constant of proportionality is dependent on the flip angle, B_0, and so on. For notational convenience, we shall neglect this scaling constant and rewrite Eq. (28) as

$$dS(x,t) = \rho(x)\,dx e^{-i\gamma(B_0+G_x x)t} \tag{29}$$

The signal in Eq. (29) is said to be frequency-encoded since its oscillating frequency $\omega(x) = \gamma(B_0 + G_x x)$ is linearly related to the spatial location. For the same reason, G_x is called a frequency-encoding gradient. The total signal received from the entire object in the presence of this gradient is

$$\begin{aligned} S(t) &= \int_{\text{object}} dS(x,t) = \int_{-\infty}^{\infty} \rho(x)e^{-i\gamma(B_0+G_x x)t}\,dx \\ &= \int_{-\infty}^{\infty} \rho(x)e^{-i\gamma G_x x t}\,dx e^{-i\omega_0 t} \end{aligned} \tag{30}$$

After demodulation (i.e., removal of the carrier signal $e^{-i\omega_0 t}$), we have

$$S(t) = \int_{-\infty}^{\infty} \rho(x)e^{-i\gamma G_x x t}\,dx \tag{31}$$

Phase-encoding is done in a similar fashion. Specifically, if we turn on a gradient G_x only for a short interval T_{pe} after an RF pulse, the local signal under the influence of this gradient is

$$dS(x,t) = \begin{cases} \rho(x)e^{-i\gamma(B_0+G_x x)t} & 0 \le t \le T_{pe} \\ \rho(x)e^{-i\gamma G_x x T_{pe}}e^{-i\gamma B_0 t}, & t \ge T_{pe} \end{cases} \tag{32}$$

It is evident that during the interval $0 \le t \le T_{pe}$, the local signal is *frequency-encoded.* As a result of this frequency-encoding, signals from different x positions accumulate different phase angles after a time interval T_{pe}. Therefore, if we use the first time interval as a preparatory period, the signal collected afterward will bear an initial phase angle

$$\phi(x) = -\gamma G_x x T_{pe} \tag{33}$$

Since $\phi(x)$ is linearly related to the signal location x, the signal is referred to as being *phase-encoded,* with G_x being the phase-encoding gradient and T_{pe} being the phase-encoding interval.

A useful insight is gained using a k-space interpretation of frequency-encoded or phase-encoded signals (13). Specifically, for the frequency-encoded signal given in Eq. (31), a simple variable substitution
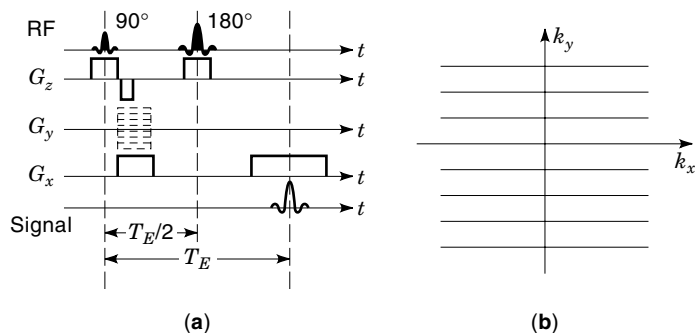
$$k_x = \gamma G_x t \tag{34}$$

Figure 8. (a) Representative 2-D Fourier imaging pulse sequence with hybrid phase and frequency-encodings and (b) its corresponding k-space sampling trajectories.

Figure 9. (a) Representative pulse sequence with 2-D frequency-encoding and (b) its corresponding k-space sampling trajectories.

will yield the following Fourier transform relationship (14):

$$S(k_x) = \int_{-\infty}^{\infty} \rho(x) e^{-i2\pi k_x x}\, dx \qquad (35)$$

In the case of phase-encoding, the same equation is obtained with the following mapping relationship:

$$k_x = \gamma\, G_x T_{pe} \qquad (36)$$

Therefore, the role of frequency-encoding or phase encoding is to map a time signal to a k-space signal. What distinguishes frequency-encoding from phase-encoding are the values that k takes. In the former case, k is a continuous function of time; but in the latter case, k is varied by changing G [or T_{pe}, as was done in the earlier days (15)].

Multidimensional Imaging

With the above localization principles, it is easy to understand how multidimensional MR imaging is done. Consider the excitation sequence shown in Fig. 8(a), which generates a set of spin-echo signals by repeatedly exciting the object with a pair of slice-selective 90° and 180° pulses (one period is shown in the figure). Each spin-echo signal is first phase-encoded with a variable G_y (16) and then frequency-encoded by G_x. It is easy to show that the imaging equation for this excitation scheme is in the form of a two-dimensional (2-D) Fourier transform (17):

$$S(k_x, k_y) = \int_{-\infty}^{\infty} \int_{-\infty}^{\infty} \rho(x,y) e^{-i2\pi(k_x x + k_y y)}\, dx\, dy \qquad (37)$$

where

$$\begin{cases} k_x = \gamma\, G_x t \\ k_y = \gamma\, G_y T_{pe} \end{cases} \qquad (38)$$

For this excitation scheme, k_y is a constant during the life span of each spin-echo signal. Therefore, each signal is mapped to a horizontal line parallel to the k_x axis. For different signals, k_y is changed so that each line assumes different locations along the k_y axis. As a result, rectilinear sampling of k space, as shown in Fig. 8(b), is achieved with this hybrid phase and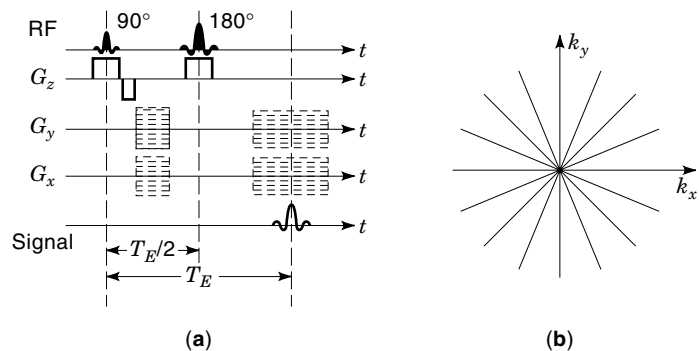 frequency-encoding scheme. In the literature, this imaging scheme is commonly known as the phase-encoding method because different time signals are phase-encoded.

Figure 9(a) shows another 2-D imaging scheme. In this scheme, each spin-echo signal is frequency-encoded by a pair of gradients: $G_{n,x} = G \cos \phi_n$ and $G_{n,y} = G \sin \phi_n$. The resulting k-space signals are given by

$$S(k \cos\phi_n, k \sin\phi_n) = \int_{-\infty}^{\infty} \int_{-\infty}^{\infty} \rho(x,y) e^{-i2\pi k(x \cos\phi_n + y \sin\phi_n)}\, dx\, dy \qquad (39)$$

where

$$\phi_n = \arctan\left(\frac{G_{n,y}}{G_{n,x}}\right) \qquad (40)$$

Therefore, each spin-echo signal is mapped to a line which runs through the origin of k space. By appropriately changing the relative strengths of the frequency-encoding gradients, one can effectively cover k space with a set of such time signals, as shown in Fig. 9(b). This 2-D frequency-encoding method is sometimes referred to as a projection-reconstruction imaging method because each data line corresponds to a projection of the underlying object according to the well-known projection-slice theorem.

To demonstrate the flexibility with data acquisition in MRI, Figs. 10(a) and 11(a) show two fast imaging sequences (18). The first is known as the echo-planar imaging (EPI) sequence (19), which acquires multiple raster lines per excitation using a fast switching gradient to form a number of gradient echoes. The second sequence samples k space in a spiral fashion through the use of time-varying gradients (20,21).
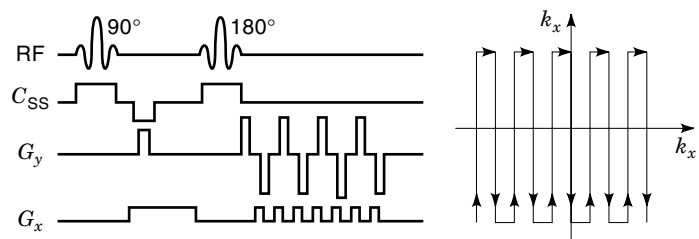

Figure 10. (a) Representative echo-planar imaging sequence and (b) its k-space sampling trajectory.

The above concepts can be extended to three-dimensional (3-D) imaging. In practice, 3-D imaging can be performed in two different modes: multislice 2-D imaging or true 3-D imaging. Although true 3-D imaging differs from multislice 2-D imaging in terms of imaging time and signal-to-noise ratio (22), the fundamental concepts for signal generation and spatial information encoding are the same. Specifically, in the former case, slice-selective pulses are used for signal generation followed by 2-D spatial information encodings. In the latter case, nonselective pulses are used to activate signal from a 3-D volume followed by spatial information encoding along all three spatial directions.

Image Reconstruction

Image reconstruction in MRI is based on two basic computational algorithms: the Fourier reconstruction algorithm and the filtered backprojection reconstruction algorithm. If k space is sampled rectilinearly, the Fourier reconstruction algorithm is used. Otherwise, filtered backprojection reconstruction is used if k space is sampled radially. For other types of k-space coverage, data interpolation is often first performed to convert the data to one of the above two types, followed by Fourier or backprojection reconstruction.

Fourier Reconstruction. Because the Fourier transform is separable, multidimensional Fourier reconstruction is implemented as cascaded 1D processing. The basic Fourier reconstruction formula is

$$\rho(x) = \Delta k \sum_{n=-N/2}^{N/2-1} S(n\Delta k)e^{i2\pi n \Delta kx} \tag{41}$$

where N is the total number of data points measured and Δk is the sampling interval. To avoid the aliasing artifact, Δk must satisfy the well-known Nyquist criterion, which states that

$$\Delta k < 1/W_x \tag{42}$$

where W_x is the object width along the x direction.

The image function $\rho(x)$ obtained from Eq. (41) will not be identical to the true image function desired because the Fourier series is truncated to N terms. As a result, the spatial resolution of $\rho(x)$ is limited to
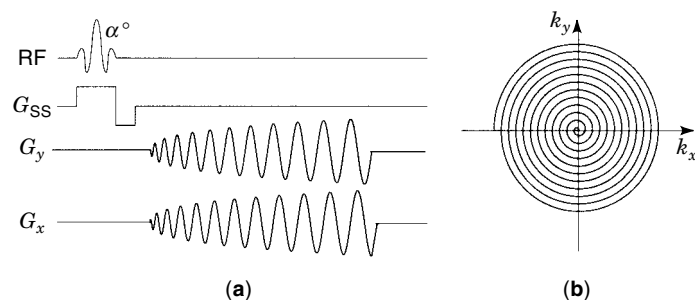
$$\Delta x = \frac{1}{N\Delta k} \tag{43}$$

Figure 11. (a) Representative spiral imaging sequence and (b) its k-space sampling trajectory.
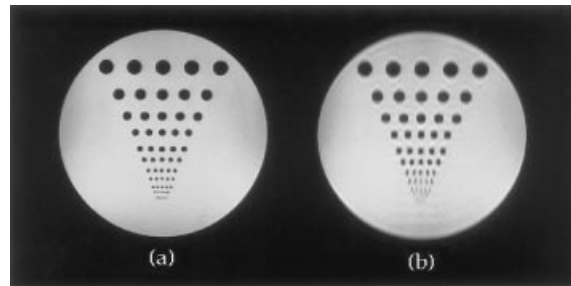

Figure 12. Illustration of the truncation artifact with Fourier reconstruction. Both images were reconstructed with 256 samples along the horizontal direction but along the vertical direction with (a) 256 samples and (b) 64 samples.

In addition, $\rho(x)$ suffers from a characteristic Gibbs ringing artifact when sharp edges are present in the object (23). This artifact manifests itself as spurious ringing around sharp edges and propagates through the entire image, as illustrated in Fig. 12.

Filtered Backprojection Reconstruction. The filtered backprojection algorithm consists of two major steps (24–26). The first step filters and Fourier transforms the k-space data along the radial direction. The second step backprojects the filtered projections obtained from the first step.

In the 2-D case, the first step is described by

$$P(r, \phi) = \int_{-\infty}^{\infty} |k|S_p(k, \phi)e^{-i2\pi kr}\, dk \tag{44}$$

where $S_p(k, \phi)$ represents the k-space data in polar form such that $S_p(k, \phi) \equiv S(k\cos\phi, k\sin\phi)$, and $P(r, \phi)$ is a filtered projection of the underlying object function $\rho(x, y)$ at an angle ϕ relative to the x axis. The subsequent step is to backproject $P(r, \phi)$ to yield the desired image $\rho(x, y)$:

$$\rho(x, y) = \int_0^{\pi} P(x\cos\phi + y\sin\phi, \phi)\, d\phi \tag{45}$$

Note that the backprojection operator, as its name implies, assigns the value of any point in $P(r, \phi)$ to the pixels on a line defined by $r = x\cos\phi + y\sin\phi$. This operation is the opposite of the projection operation.

Similar to Eqs. (44) and (45), the 3-D backprojection reconstruction algorithm is described by the following two equations:

$$P(r, \theta, \phi) = \int_{-\infty}^{\infty} k^2 S_p(k, \theta, \phi)e^{-i2\pi kr}\, dk \tag{46}$$

and

$$\rho(x, y, z) = \int_0^{2\pi} \int_0^{\pi} P(x\sin\theta\cos\phi + y\sin\theta\sin\phi + z\cos\theta, \theta, \phi)\sin\theta\, d\theta d\phi \tag{47}$$

In practical implementation, the above equations are discretized. In addition, to minimize noise amplification by the high-pass filters $|k|$ or k^2, other more practical filter functions
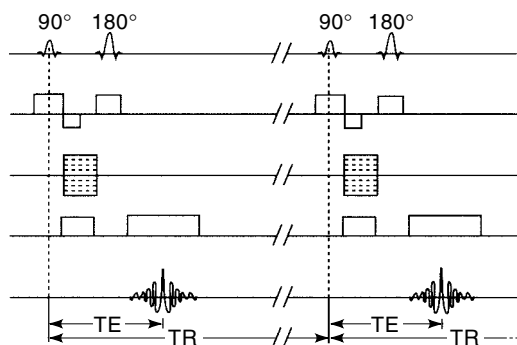
Figure 13. Representative saturation-recovery spin-echo sequence.

are also often used. The 3-D filtered backprojection algorithm can be implemented in a two-stage fashion. At each stage, 2-D filtered backprojection is performed. Detailed discussion can be found in Refs. 27 and 28.

IMAGE CONTRAST MECHANISMS

Image contrast is an important imaging parameter. Good image contrast is useful not only for a clear definition of anatomical structures but also for differentiation between normal and diseased tissues. The MR image pixel value is, in general, dependent on a host of intrinsic parameters including the nuclear spin density ρ, the spin-lattice relaxation time T_1, the spin–spin relaxation time T_2, molecular motions (such as diffusion and perfusion), susceptibility effects, and chemical shift differences. The imaging effects of these parameters can be suppressed or enhanced in a specific experiment by another set of operator-selectable imaging parameters, such as repetition time (T_R), echo time (T_E), flip angle (α), and so on. If the data acquisition parameters are chosen such that the T_1 effect is dominant, the resulting image is said to carry a T_1 contrast or T_1 weighting. Similarly, we have spin density contrast or T_2 contrast.

To see this, we consider the saturation-recovery spin-echo sequence consisting of a string of equally spaced $90°–\tau–180°$ pulses as illustrated in Fig. 13. The time interval between two successive 90° pulses is called the repetition time (T_R). Based on the relaxation behavior described in Eq. (14), the longitudinal magnetization after the $(n-1)$th pulse but just

before the nth pulse is given by

$$M_z^{(n)}(90°-) = M_z^0(1 - e^{-T_R/T_1}) + M_z^{(n-1)}(90°+)e^{-T_R/T_1}, \quad (48)$$

where $n > 1$. For this excitation sequence, it is usually assumed that

$$M_z^{(n)}(90°+) = 0, \qquad n \geq 1 \qquad (49)$$

which is known as the *saturation condition*. Equation (48) can then be written as

$$M_z^{(n)}(90°-) = M_z^0(1 - e^{-T_R/T_1}), \qquad n \geq 2 \qquad (50)$$

which means that the spin system reaches a "steady state" by the time the second 90° pulse is applied. For this reason, the first 90° pulse is sometimes called the preparatory pulse and the corresponding signal is often discarded.

From Eq. (50), we obtain

$$M_{xy}^{(n)}(90°+) = M_z^0(1 - e^{-T_R/T_1}), \qquad n > 1 \qquad (51)$$

and the amplitude of the spin-echo signal becomes

$$A_{\text{echo}} = M_z^0(1 - 2e^{-(T_R-T_E/2)/T_1} + e^{-T_R/T_1})e^{-T_E/T_2} \qquad (52)$$

In practice, $T_E \ll T_R$ and the above expression can be simplified to

$$A_{\text{echo}} = M_z^0(1 - e^{-T_R/T_1})e^{-T_E/T_2} \qquad (53)$$

The signal expression in Eq. (53) indicates that the image intensity of this excitation sequence carries simultaneously a T_1 weighting, a T_2 weighting, and a spin-density weighting. However, one can selectively emphasize one of these weightings by properly choosing the sequence parameter T_R and T_E. For instance, if a short T_E is used, the term $\exp(-T_E/T_2)$ approaches 1 and the T_2-weighting factor can then be ignored. Similarly, if a long T_R is used, the T_1-weighting factor will drop out.

The above discussion can be extended to the inversion-recovery spin-echo sequence shown in Fig. 14. Correspondingly to Eq. (53), one can derive for the inversion-recovery sequence that

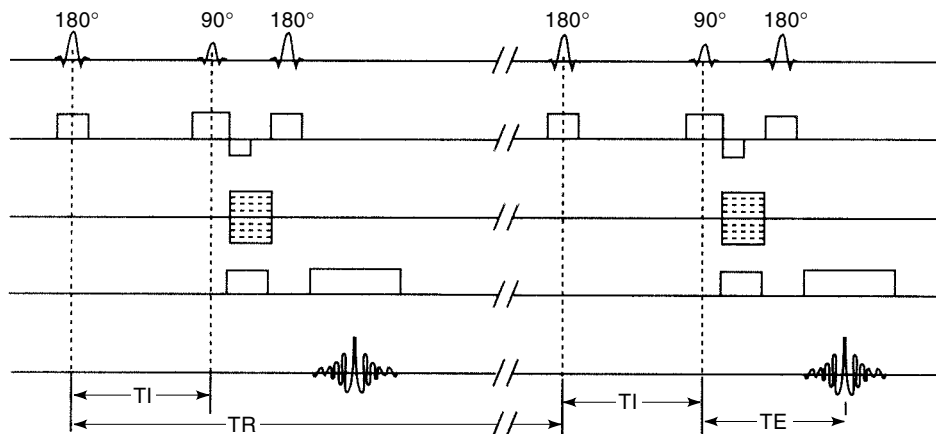$$A_{\text{echo}} = M_z^0(1 - 2e^{-T_I/T_1} + e^{-T_R/T_1})e^{-T_E/T_2} \qquad (54)$$

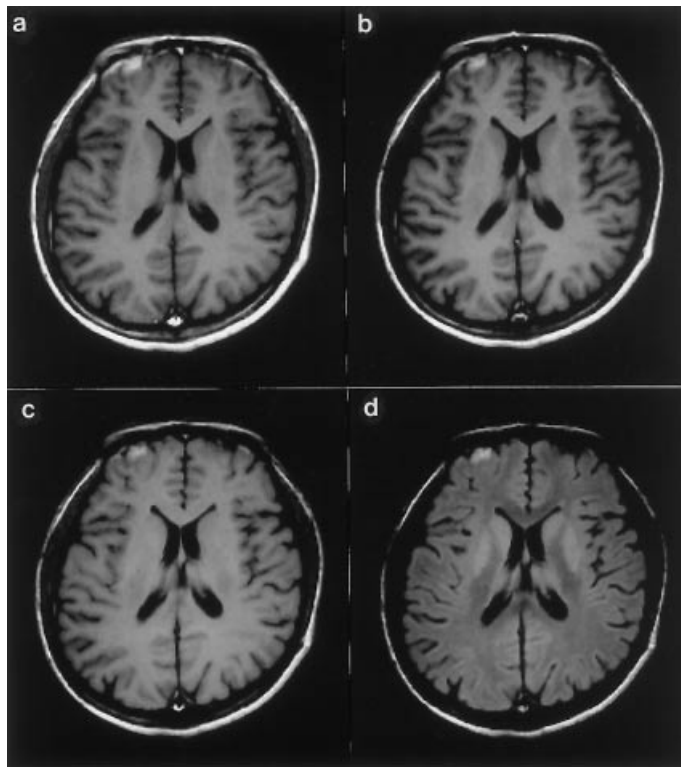**Figure 14.** Representative inversion-recovery spin-echo sequence.

Figure 15. Transaxial head images as a function of T_R: (a) $T_R = 250$ ms, (b) $T_R = 500$ ms, (c) $T_R = 1000$ ms, and (d) $T_R = 2000$ ms. The shorter T_R images are heavily T_1-weighted, while the long T_R image is more proton-density-weighted. Note that the contrast between the white matter and gray matter reverses from the shortest to the longest T_R.

which indicates that this sequence can generate T_1-weighted, T_2-weighted, and spin-density-weighted contrast as does the saturation-recovery spin-echo sequence.

In contrast to the saturation-recovery sequence, we now have two sequence parameters, T_I and T_R, to adjust for optimal T_1 contrast. Specifically, by properly choosing the inversion time interval, one can force some tissue components to take on negative or even zero intensities. For example, if T_I is set to the value

$$T_I = [\ln 2 - \ln(1 + e^{-T_R/T_1})]T_1 \qquad (55)$$

then

$$1 - 2e^{-T_I/T_1} + e^{-T_R/T_1} = 0 \qquad (56)$$

and the corresponding tissue component will be nulled. This is known as the signal-nulling effect.

To illustrate the concept of tissue contrast as a function of data acquisition parameters, two sets of axial head images, acquired using a saturation-recovery spin-echo sequence with different T_1 and T_2-weightings, are shown in Figs. 15 and 16. The imaging parameteres were field of view (FOV): $\text{FOV}_x = 256$ mm and $\text{FOV}_y = 192$ mm, and number of encodings: $N_x = 256$ and $N_y = 192$. One can appreciate the image appearance changes due to different acquisition parameters.

As a final example, we consider the contrast behavior of a basic gradient-echo imaging sequence shown in Fig. 17. As-
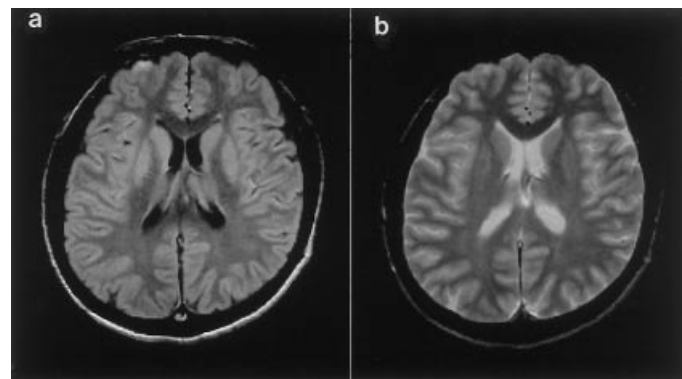

Figure 16. Transaxial head images obtained from the same physical location as in Fig. 15. Two different echo times were used: $T_E = 20$ ms in (a) and $T_E = 80$ ms in (b), with the same $T_R = 2000$ ms. Image (a) is heavily proton-density-weighted, while image (b) is T_2-weighted.

suming that $T_R \gg T_2$ such that $M_{xy}(T_R) = 0$, one can shown that the echo amplitude, after dynamic equilibrium is reached, is given by

$$A_{\text{echo}} = \frac{M_z^0(1 - e^{-T_R/T_1})}{1 - \cos\alpha e^{-T_R/T_1}} \sin\alpha e^{-T_E/T_2^*} \qquad (57)$$

Equation (57) clearly shows that the image intensity from this gradient-echo sequence carries both T_1 and T_2^* weightings. The T_2^*-weighting factor is characteristic of a gradient-echo sequence, and it is controllable by adjusting the echo time T_E. This is similar to the way in which the T_2 contrast is adjusted in a spin-echo imaging sequence. However, in contrast to that in a spin-echo sequence, the T_1 contrast in the gradient-echo sequence is dependent on both the flip angle α and the repetition time T_R. Specifically, when α is small, $\cos\alpha \approx 1$ and consequently the T_1-weighting factor is eliminated. As the flip angle is increased for a given T_R, the T_1-weighting factor becomes more significant. To further illustrate this concept, a set of brain images acquired with differ-
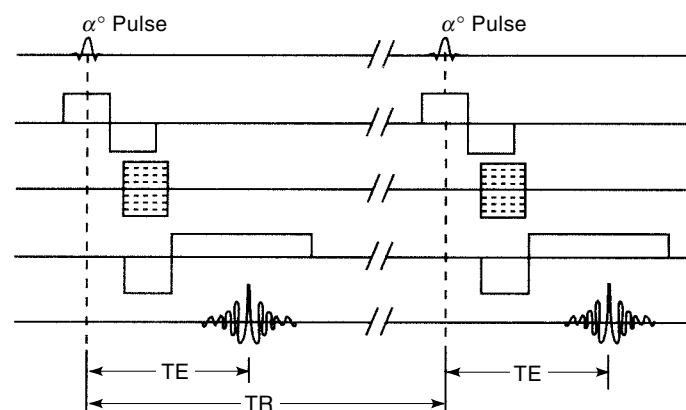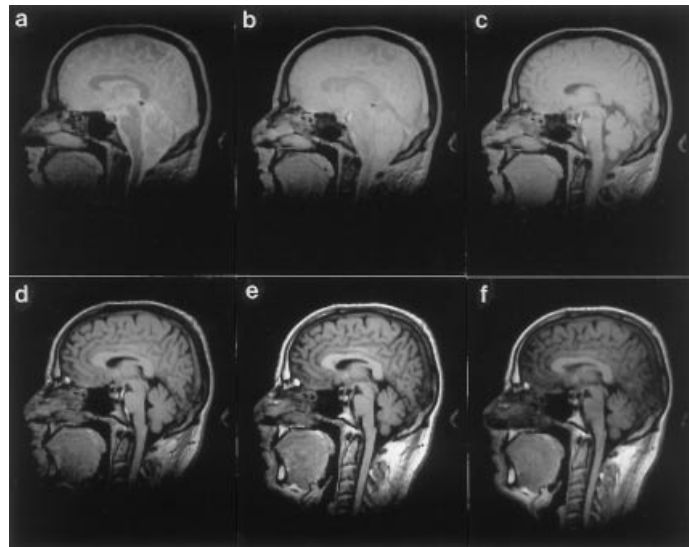

Figure 17. Generic gradient-echo imaging sequence.

Figure 18. Brain images acquired using a gradient-echo sequence ($T_R = 25$ ms, $T_E = 4.75$ ms) with different flip angles: (a) $\alpha = 2°$, (b) $\alpha = 5°$, (c) $\alpha = 10°$, (d) $\alpha = 20°$, (e) $\alpha = 40°$, and (f) $\alpha = 60°$. Note that at small flip angles the images show the characteristics of proton density weighting, whereas at larger flip angles the T_1 weighting becomes dominant. Each of these images is acquired from a 3D data set with $N_x = 512$, $N_y = 512$, $N_z = 80$, $FOV_x = 256$ mm, $FOV_y = 256$ mm, and $FOV_z = 160$ mm. The image in (a) was obtained by averaging two slices to improve SNR. (Images courtesy of Ramesh Venkatesan.)

Figure 19. One slice from a 128-slice 3-D TOF acquisition is shown in (a). The image in (b) was created by performing a maximum intensity projection (MIP) operation through 64 slices, which picks out the peak signal along any ray in the viewing direction. As can be seen, the arterial blood is clearly visible for the major vessels in the brain. The imaging parameters used were $T_R = 35$ ms, $T_E = 6$ ms, flip angle $\alpha = 25°$, and a resolution of $0.28 \times 0.28 \times 1$ mm³. (Images courtesy of Ramesh Venkatesan.)

ent flip angles is shown in Fig. 18. As can be seen, at small flip angles the images show mainly the proton density distribution with cerebral spinal fluid having the highest intensity, followed by gray matter and white matter. At larger flip angles, the images become T_1-weighted.

APPLICATION EXAMPLES

MR imaging is a very flexible technique. It has been used for both anatomical and functional imaging applications. This section gives the reader a sampling of some of these applications by looking at 3-D magnetic resonance angiography, cardiovascular imaging, and functional brain imaging.

MR Angiography

The method of data acquisition described so far is for stationary spins. MR signals are known to be sensitive to flow. MR angiography (MRA) is a technique to exploit this property to image vascular structures and/or measure flow (29). Two distinct types of flow effects have been used for MRA: time-of-flight effects (spin motion between RF pulses) and phase effects (spin motion in the presence of a gradient field), which are discussed next.

Time-of-Flight MRA. Time-of-flight (TOF) MRA is a popular clinical method to image blood flow. This method uses the motion of the blood to enhance its signal. Consider the mechanism of how the signal is generated in an MRI experiment. The local spins being imaged experience multiple RF pulses, one for each phase encoding step. These pulses lead to a suppression of the signal, as can be understood from the discus-
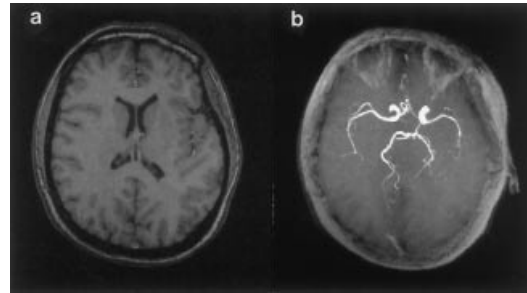
sion in the previous sections. Imagine a thin slab of tissue which is excited and through which blood flows orthogonally to the imaging plane. If the distance the blood travels is greater than the slice thickness, then the blood that is present for a given RF pulse has never seen the previous pulse, and hence its signal is not saturated. For thicker slices, this analogy will not be completely true, but for 3-D imaging, the slices near the incoming edge of the excited slab will have the brightest blood and the slices on the far side will have the darkest blood. For fast-flowing blood in vessels like arteries, even slabs 5 cm thick still reveal blood brighter than the background tissue. The blood in the veins, on the other hand, has traveled through the region of interest as arterial blood and is usually naturally saturated.

This TOF approach is demonstrated in Fig. 19(a), where blood is seen to be bright on a single image from a 3-D data set, and in Fig. 19(b), where the entire 3-D data set is projected onto a single viewing plane. TOF MRA is very dependent on the actual flow rate; and although it is very commonly used and often very good, it can lead to saturation of blood. The use of a T_1 reducing contrast agent can eliminate this dependence on flow because T_1 of all blood is dramatically reduced, making the signal bright on short T_R, T_1-weighted im-
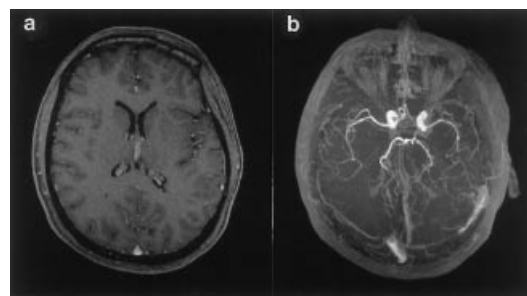

Figure 20. Saturation of blood in TOF methods can still cause some ambiguities in the clinical interpretation of MRA data. For this reason, a contrast agent is often used to enhance the signal from the blood. A 3-D MIP over 64 slices in the same volume, as in Fig. 19, shows the enhancement of all vessels. A larger-than-usual flip angle (25°) was used because of the short T_R the blood has inherited. (Images courtesy of Ramesh Venkatesan.)
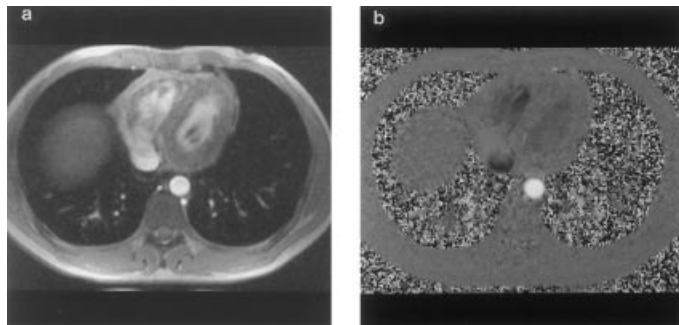
Figure 21. Phase contrast MRA images through the vessels in the thorax show how well background tissue is eliminated and the flow information in the vessels is illuminated at any given point in the cardiac cycle. The bright vessel is the aorta. Shown here are (a) the magnitude image and (b) the phase image. The data were acquired with a five-segment cardiac-gated data set using $T_R = 21.2$ ms. This means that a flow image is available every 106 ms in the cardiac cycle. The imaging parameters were $T_E = 5$ ms, $\alpha = 30°$, $\text{FOV}_x = \text{FOV}_y = 256$ mm, $N_x = 256$, $N_y = 128$, and slice thickness $\Delta z = 6$ mm. (Images courtesy of Debiao Li.)

ages (see Fig. 20) and independent of its flow characteristics. For this reason, this new 3-D method is likely to prove the most reliable.

Phase Contrast MRA. Phase contrast MRA is based on the phase change that the transverse magnetization of moving spins experience relative to that of their stationary counterparts. To understand this effect, consider the phase accumulation of stationary spins and moving spins in the presence of a gradient G_x. It is easy to show that stationary spins at location x accumulate a phase $\phi = \omega t = \gamma G_x x t$, while spins moving at velocity v along the gradient direction will accumulate a bigger phase $\phi = \gamma G(xt + vt^2/2)$. Hence, moving spins can be recognized on the basis of the extra phase shift that they accumulate.

How much spins have dephased during the data acquisition window is dependent on the readout gradient as a function of time. For example, it is possible to design the gradient waveform such that its nth-order moments are zero at the peak of the echo signal. That is,

$$\int t^n G_x(t)\,dt = 0, \qquad n = 0, 1, \ldots \qquad (58)$$

These are called flow-compensation conditions, and in practice we are usually concerned with the zeroth and first moments. Specifically, if the first moment is not zero, spins with various velocities across a vessel lumen dephase, and little or no signal from the blood appears in the image. For phase contrast MRA, two data sets are often acquired, one with and one without a flow-encoding gradients. Complex subtraction of the two data sets will then give an image of the vascular tissues "free" of the stationary background structures. An example of flow in the aorta and vena cava is shown in Fig. 21.
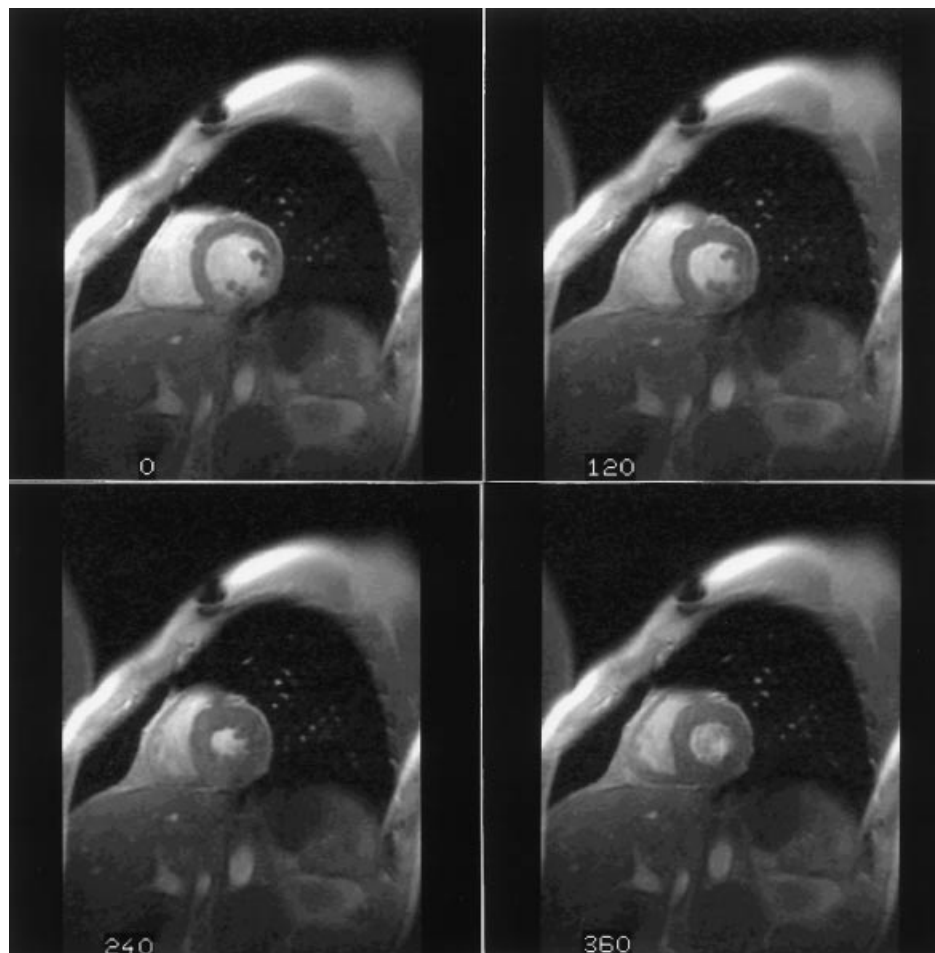

Figure 22. Cine imaging is a means to visualize cardiac motion during the cardiac cycle. In this figure, a series of four images is extracted from a total of 12 images acquired during the cardiac cycle with $T_R = 60$ ms. A five-segment breath-hold method was used with cardiac gating. The imaging parameters were $T_E = 5$ ms, $\alpha = 20°$, $\text{FOV}_x = \text{FOV}_y = 350$ mm, $N_x = 256$, $N_y = 128$, and 8 mm slice thickness. (Images courtesy of Debiao Li.)
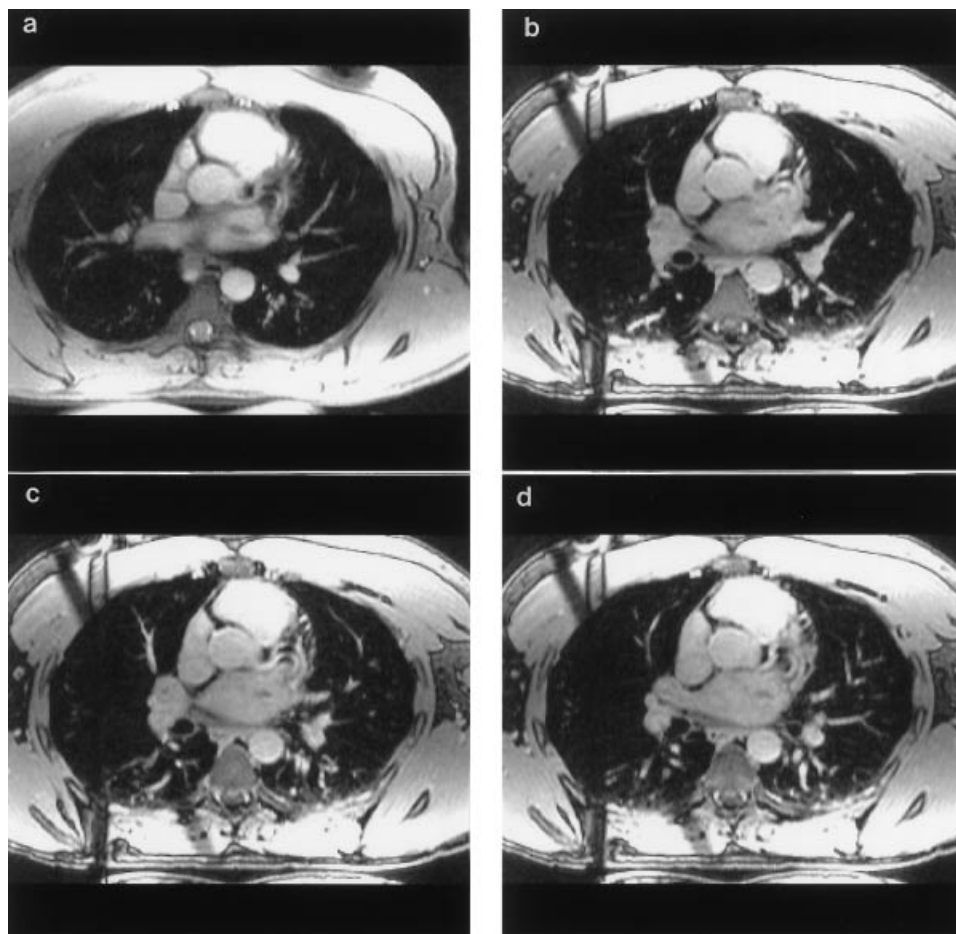
Figure 23. Images of the coronary artery. (a) A 2-D data set of the left main coronary vessel. (b–d) Three adjacent slices from a 3-D data set. The imaging parameters for the 2-D experiment were T_E = 6.2 ms, T_R = 6.2 ms, FOV$_x$ = 300 mm, FOV$_y$ = 225 mm, N_x = 256, N_y = 110, and 4 mm slice thickness. The imaging parameters for the 3-D parameters were T_E = 2.7 ms, T_R = 8 ms, FOV$_x$ = 300 mm, FOV$_y$ = 225 mm, N_x = 256, N_y = 96, and 2 mm slice thickness. (Images courtesy of Jie Zheng.)

Cardiovascular Imaging

MRI is becoming an important tool for studying cardiac function and diagnosing cardiovascular diseases (30). Using flow-compensated gradient-echo imaging sequences and cardiac gating, it is now possible to obtain dynamic images from a beating heart with high spatial and temporal resolution. These images are often viewed in cine format to visualize the global cardiac motion, thus the name cine imaging. An example of cine cardiac imaging is illustrated in Fig. 22, in which a series of four images from a cine set is shown.

Fast imaging has also been extended along with the above mentioned MRA capabilities to create images of the coronary arteries using either fast 2-D breath-hold or fast 3-D imaging techniques. Figure 23(a) shows an example of a 2-D breath-hold image of a section of the heart containing the left coronary artery. Figure 23(b–d) shows three slices from a 3-D data set showing the same vessel. One of the advantages of using a 3-D method is that a series of thin contiguous slices can be acquired. Another advantage is that when the region of interest is not exactly in plane, it is possible to reformat the data so that it appears as if it is in plane (this processing is referred to as multiplanar reconstruction).

Functional Brain Imaging

Functional MRI (fMRI) is a class of new techniques developed in the last few years to image MR signal changes related to neuronal activity (31). Since changes in neuronal activity are accompanied by local changes in cerebral blood flow (CBF), blood volume (CBV), blood oxygenation, and metabolism, various pulse sequences have been developed to capture these physiological changes in MR signals to produce what are called functional maps of cognitive tasks (32).

The original *Science* article (31) on fMRI showed functional maps acquired in the presence of a contrast agent. More recent methods exploit blood-oxygenation-level-dependent (BOLD) signal changes (33,34). It is known that venous blood has a different local magnetic field than arterial blood because it has a higher concentration of deoxyhemoglobin, which is paramagnetic. This difference can be captured in complex gradient-echo images whose phase is directly proportional to the local magnetic field.

Figure 24 shows an example of fMRI with a simple mental task—that is, moving the fingers of the right hand. In this experiment, the region by the primary motor cortex in the left part of the brain responds by changing the local blood flow while not significantly increasing its consumption of oxygen. This decoupling of the local metabolism with flow leads to a reduced concentration of the venous deoxyhemoglobin (an increase in oxygen saturation) and, hence, a reduction of the local magnetic field. This results in a change in the signal intensity in the associated pixels in the motor cortex region. Furthermore, the reduced field will also cause the local T_2 of blood to increase, and this also leads to a signal increase. Upon subtraction with the original resting-state image, the excited region can be visualized.
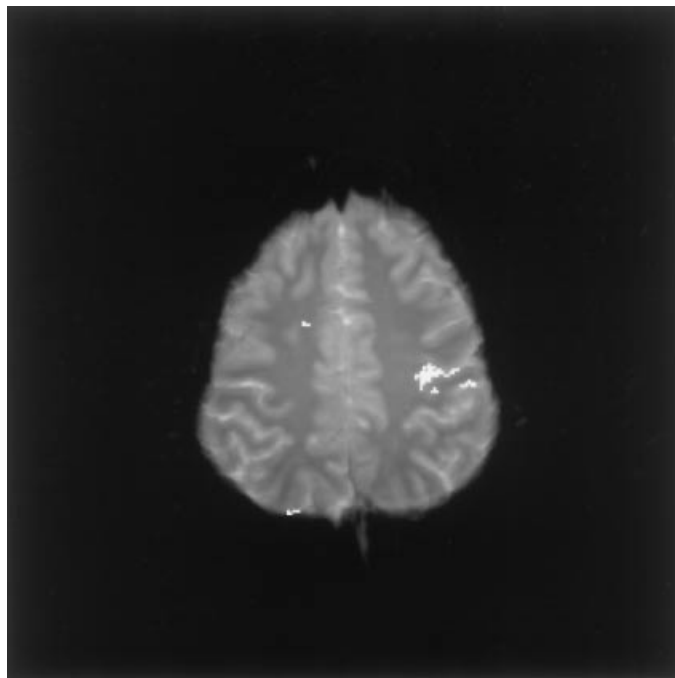
Figure 24. Illustration of functional brain imaging with a motor task. A gradient-echo sequence with an echo time of 79 ms was used to collect data during resting state (no finger motion) and activated state (movement of the fingers of the right hand). Subtracting the former from the latter yields an activation region, which is shown as an overlay on one of the original anatomical images. As expected, the activation region sits in the area of the primary motor cortex. The imaging parameters were $T_R = 5$ s, $\alpha = 90°$, $FOV_x = FOV_y = 206$ mm, $N_x = 256$, $N_y = 192$, and 5 mm slice thickness. (Images courtesy of Karthik Kuppusamy.)

CONCLUSION

Magnetic resonance imaging is a powerful imaging modality. It is capable of imaging the structure, metabolism, and function of a biological object. While an incredible array of methods and applications have been developed in the last two decades, the technology is still far from maturation. Technological developments will continue to improve the speed, efficiency, and accuracy of the imaging method. These technical improvements will further enhance the practical utility of the method for many important applications ranging from 3-D cardiac imaging to functional brain mapping.

BIBLIOGRAPHY

1. E. M. Purcell, H. C. Torrey, and R. V. Pound, Resonance absorption by nuclear magnetic moments in a solid, *Phys. Rev.,* **69**: 37–38, 1946.

2. F. Bloch, Nuclear induction, *Phys. Rev.,* **70**: 460–474, 1946.

3. P. C. Lauterbur, Image formation by induced local interactions: Examples employing nuclear magnetic resonance, *Nature,* **242**: 190–191, 1973.

4. D. D. Stark and W. G. Bradley, Jr., *Magnetic Resonance Imaging,* Vols. 1 and 2, 2nd ed., St. Louis: Mosby–Year Book, 1992.

5. A. C. Kak and M. Slaney, *Principles of Computerized Tomographic Imaging,* New York: IEEE Press, 1988.

6. C. P. Slichter, *Principles of Magetic Resonance,* 3rd ed., New York: Springer-Verlag, 1990.

7. A. Abragam, *Principles of Nuclear Magnetism,* Oxford, UK: Oxford Univ. Press, 1989.

8. W. S. Hinshaw and A. H. Lent, An introduction to NMR imaging: From the Bloch equation to the imaging equation, *Proc. IEEE,* **71**: 338–350, 1983.

9. C.-N. Chen and D. I. Hoult, *Biomedical Magnetic Resonance Technology,* New York: Adam Hilger, 1989.

10. E. L. Hahn, Spin echoes, *Phys. Rev.,* **80**: 580–594, 1950.

11. S. Meiboom and D. Gill, Modified spin-echo method for measuring nuclear relaxation times, *Rev.Sci. Instrum.,* **29**: 669–691, 1958.

12. A. A. Maudsley and G. B. Matson, Selective excitation in MRI, in D. M. Grand and R. K. Harris (eds.), *Encyclopedia of Nuclear Magnetic Resonance,* Vol. 7. Chichester, England: Wiley, 1995, pp. 4210–4218.

13. D. B. Twieg, The *k*-trajectory formulation of the NMR imaging process with applications in analysis and synthesis of imaging methods, *Med. Phys.,* **10**: 610–621, 1983.

14. R. N. Bracewell, *The Fourier Transform and Its Applications,* New York: McGraw-Hill, 1978.

15. A. Kumar, D. Welti, and R. Ernst, NMR Fourier zeugmatography, *J. Mag. Reson.,* **18**: 69–83, 1975.

16. W. A. Edelstein et al., Spin warp NMR imaging and applications to human whole-body imaging, *Phys. Med. Biol.,* **25**: 751–756, 1980.

17. Z. H. Cho et al., Fourier transform nuclear magnetic resonance tomographic imaging, *Proc. IEEE,* **70**: 1152–1173, 1982.

18. F. W. Wehrli, *Fast-Scan Magnetic Resonance: Principles and Applications,* New York: Raven Press, 1991.

19. P. Mansfield and P. G. Morris, *NMR Imaging in Biomedicine,* New York: Academic Press, 1982.

20. A. Macovski, Volumetric NMR imaging with time-varying gradients, *Magn. Reson. Med.,* **2**: 29–40, 1985.

21. A. B. Ahn, J. H. Kim, and Z. H. Cho, High speed spiral-scan echo planar NMRV imaging—I, *IEEE Trans. Med. Imaging,* **MI-5**: 1–6, 1986.

22. J. Carlson et al., Signal-to-noise ratio and section thickness in two-dimensional versus three-dimensional Fourier transform MR imaging, *Radiology,* **166**: 266–270, 1988.

23. R. M. Henkelman and M. J. Bronskill, Artifacts in magnetic resonance imaging, *Rev. Magn. Reson. Med.,* **2** (1): 1–126, 1987.

24. Z.-P. Liang et al., Constrained reconstruction methods in MR imaging, *Rev. Magn. Reson. Med.,* **4**: 67–185, 1992.

25. S. R. Deans, *The Radon Transform and Some of Its Applications,* New York: Wiley, 1983.

26. G. T. Herman, *Image Reconstruction from Projection: The Fundamentals of Computerized Tomography,* New York: Academic Press, 1980.

27. W. B. Hyslop, R. K. Woods, and P. C. Lauterbur, Four-dimensional spectra-spatial imaging using projection reconstruction, *IEEE Trans. Med. Imaging,* **14**: 374–383, 1995.

28. Z.-P. Liang and D. C. Munson, Partial Radon transforms, *IEEE Trans. Image Process.,* **6**: 1467–1469, 1997.

29. E. J. Potchen et al., *Magetic Resonance Angiography: Concepts and Applications,* St. Louis: Mosby–Year Book, 1993.

30. E. M. Haacke, D. Li, and S. Kaushikkar, Cardiac MR imaging: Principles and techniques, *Topics Magn. Reson. Imaging,* **7**: pp. 200–217, 1995.

31. J. W. Belliveau et al., Functional mapping of the human visual cortex by magnetic resonance imaging, *Science,* **254**: 716–719, 1991.

32. S.-G. Kim and K. Ugurbil, Functional magnetic resonance imaging of the human brain, *J. Neurosci.,* **74**: 229–243, 1997.

33. K. R. Thulborn et al., Oxygenation dependence of the transverse relaxation time of water protons in whole blood at high field, *Biochim. Biophys. Acta,* **714**: 265–270, 1982.

34. S. Ogawa et al., Brain magnetic resonance imaging with contrast dependent on blood oxygenation, *Proc. Natl. Acad. Sci. USA,* **87**: 9868–9872, 1990.

Z.-P. LIANG
University of Illinois at Urbana-
    Champaign
E. M. HAACKE
Washington University